"Untangling the mechanics and topology in the frictional response of long overhand elastic knots"
— Supplemental Information —

M.K. Jawed, P. Dieleman, B. Audoly, P. M. Reis

S1 Experimental details

In this section, we provide specific information on our experimental apparatus. For all of our experiments we used a universal testing machine (Instron 5943, Norwood, MA) with a 10 N low-profile static load cell (2530 from the same manufacturer). The displacement and force resolutions were 10^{-4} mm and 10^{-4} N, respectively. Our experiments involved measuring displacements and forces of $\sim 10^2$ mm and ~ 1 N. The knots were tied in Nitinol rods (Nitinol Devices and Components, Inc). The material of the rod was superelastic Nitinol alloy SE508 with Young's modulus, $E = 67.50 \pm 0.25$ GPa, that was determined by a tension test where the force signature from a gradually imposed extension on a straight rod in the universal testing machine was recorded using a 1 kN load cell. As mentioned in the main text, one extremity of the rod was clamped to a base that was fixed to the lab frame and the other end was attached to the load cell of the universal testing machine. The rotation of the rod at both the ends was fixed. The rod was aligned vertically (along the direction of gravity) during the tests; however, the weight of the rod was negligible compared with the registered force signatures. All the force vs. extension measurements reported in the main text are reproducible which we ensured by repeating the experiments at least 3 times. We also performed representative experimental trials at different extension rates, $\dot{e} = \{0.5, 1.0, 2.0\}$ mm/s, and did not find any systematic deviation. The experiments reported in the manuscript use a rate of $\dot{e} = 1$ mm/s.

S2 Summary of scaling assumptions

We review the various approximations made in the main text, and identify the asymptotic regime in which our analysis applies. We assumed $n \gg 1$ and $\epsilon \ll 1$. We obtained a helical step $2\pi/k \sim \sqrt{h\,R} \sim h/\epsilon$. As the topological (unknotting) number n was assumed to be large ($n \gg 1$), the braid's length is given by a different (larger) length-scale $\ell \sim n\,h/\epsilon$. Note that the separation of scales mentionned in the main text, $h \ll \frac{\ell}{n} = \frac{2\pi}{k} \sim \frac{h}{\epsilon} \ll R \sim \frac{h}{\epsilon^2}$, follows from these assumptions.

We also assumed that the braid, which is subjected to a tensile force F from the tail and a bending moment $\sim B/R$ from the loop, stays almost straight; calling w the typical deflection of the braid, and equating the typical moments $F\,w \sim B/R$, this yields a typical slope angle $w/\ell \sim \frac{B}{R\,F\,\ell}$. For this angle to be indeed small, we need $F \gg \frac{B}{R\,\ell}$. Inserting the expressions of F and k found in the main text, this yields $\mu \gg \frac{1}{n^2}$. Finally, we assumed that both strands had the same helical radius h everywhere along the braid, even though the tension in each strand decreases from the value F exerted on the tails to a much smaller value near the loop (as a result of friction). For this variation ($\sim F$) of the tensile force along the braid to have no influence on the pitch of the helix, it is required that F is much smaller than the characteristic internal force Bhk^3 that builds up in a helical rod, *i.e.* $F \ll Bhk^3$. Inserting the expression for F found in Eq. (4) of the main text into this inequality, yields $\mu\,n\,B\,h\,k^3 \ll B\,h\,k^3$, such that $\mu \ll \frac{1}{n}$. To sum up, our analysis is valid in the asymptotic limit $\epsilon \ll 1$, $n \gg 1$ and $\frac{1}{n^2} \ll \mu \ll \frac{1}{n}$.

Having characterized the asymptotic regime where our model applies, we now return to the dimensionless number $\frac{F}{B\,k^2}$ introduced in the main text. This number is the ratio of the lineic density of normal force predicted by the string model to the lineic density of normal force due to the bending stiffness in the braid. Using Eq. (4) of the main text, we have $\frac{F}{B\,k^2} \sim \mu n h k \sim (\mu n)\epsilon$ which is the product of two small numbers by our scaling assumptions, such that $\frac{F}{B\,k^2} \ll 1$. This confirms that the contact force P arises primarily from the stiffness of the filament, as we have assumed in the main text.

S3 The nonlinear Elastica problem for the loop

To analyze the loop, we work in units such that $R = 1$. The problem shown in Fig. S1(a) allows one to find the relation between the braid length, ℓ, and the curvilinear length, λ, of the loop.

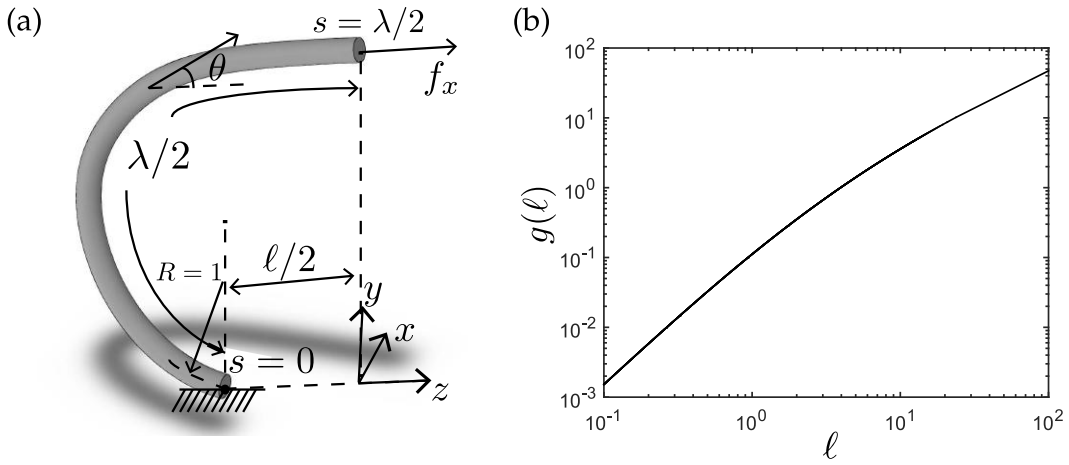

Figure S1: (a) The non-linear Elastica problem for the outer solution of the loop that emanates from the braid. (b) The function g that maps $\frac{\ell}{R}$ to $\frac{\ell^2}{eR}$, here with $R = 1$.

We work in the plane (z, y). We define the slope angle θ such that the tangent is $\cos\theta\,\mathbf{e}_z + \sin\theta\,\mathbf{e}_y$. By symmetry, the constant internal force, $\mathbf{f}$, is along the z axis supporting the braid: $f_y = 0$. The equilibrium of the half-loop is formulated as an Elastica problem, $B\,\theta'' - f_z\,\sin\theta = 0$ with boundary conditions $\theta(0) = \pi$, $\theta'(0) = -1/R = -1$, and $\theta(\lambda/2) = 0$. Let $\overline{f} = f_x/B$ be the dimensionless internal force. Using the conserved energy and some of the boundary conditions, the equilibrium shape of the Elastica is reduced to a problem of quadrature,

$$\mathrm{d}S = \frac{-\mathrm{d}\theta}{\sqrt{1 - 2\,\overline{f}\,(1 + \cos\theta)}}. \tag{S1}$$

Integration of Eq. (S1) yields

$$\lambda(\overline{f}) = 2\int \mathrm{d}S = \int_0^{\pi} \frac{2\,\mathrm{d}\theta}{\sqrt{1 - 2\,\overline{f}\,(1 + \cos\theta)}} = 4\,K(4\,\overline{f}) \tag{S2a}$$

$$\ell(\overline{f}) = 2\int \cos\theta\,\mathrm{d}S = \int_0^{\pi} \frac{2\,\cos\theta\,\mathrm{d}\theta}{\sqrt{1 - 2\,\overline{f}\,(1 + \cos\theta)}} = \frac{2\left((1 - 2\,\overline{f})\,K(4\,\overline{f}) - E(4\,\overline{f})\right)}{\overline{f}}, \tag{S2b}$$

where K and E denote the complete elliptic integrals of the first and second kind, respectively. Recall that we work is in units such that $R = 1$, and that e was defined as $e = \lambda + \ell$. The function g which maps $\frac{\ell}{R}$ to

$\frac{\ell^2}{Re}$ is then found as the graph of the curve $\left(\ell, \frac{\ell^2}{\lambda+\ell}\right)$ parameterized by $\overline{f}$: this yields the following definition of g

$$g(\ell) = \frac{\ell^2}{4\,K(4\,\overline{f}(\ell)) + \ell} \tag{S3}$$

in terms of $\overline{f}(\ell)$, the inverse of the function $\ell(\overline{f})$ defined in Eq. (S2b). Note that the argument ℓ of g will be replaced with $\frac{\ell}{R}$ when we no longer work with a set of units such that $R = 1$.

In Fig. S1(b), we obtain a plot of the function $g = \ell/e$ as a function of ℓ by actually doing a parametric plot of $\left(\ell(\overline{f}), \lambda(\overline{f})\right)$ for $0 < \overline{f} < \frac{1}{4}$ (this is the range of values of $\overline{f}$ where the integrands in Eqs. (S2) are defined): the parametric plot is much easier to obtain than the regular plot based on Eq. (S3) as it does not require the inverse function $\overline{f}(\ell)$. The theoretical prediction plotted as the dashed line in Fig. 4 of the main text has similarly been obtained as the parametric curve $\left(\frac{1}{8\sqrt{3}\,\pi^3}\,\frac{\ell^2(\overline{f})}{\lambda(\overline{f})+\ell(\overline{f})}, \frac{\mu}{96\sqrt{3}\,\pi^2}\,\ell^3(\overline{f})\right)$, plotted in log-log scale, based on Eqs. (S2).

S4 Shape of the knots at high values of the unknotting number

In Fig. S2, we provide representative photographs of knots on the Nitinol rod (geometric and material properties were specified in the main text) at high values of the unknotting number, $n = \{8, 9, 10\}$. Note that this Nitinol rod was used in all of the quantitative experiments reported in the main text, except in Fig.1a-d, where photographs of a piece of rope (5 mm diameter) were presented for illustration purposes (as stated in the caption of Fig 1). Despite the complex shapes of the knots and large aspect ratios of their braids at these high values of n, it is remarkable that the theoretical framework summarized by Eq. (5) of the main text is in such good agreement with the experimental data (see Fig. 5 of the main text), across a wide range of the unknotting number, $1 \leq n \leq 10$.

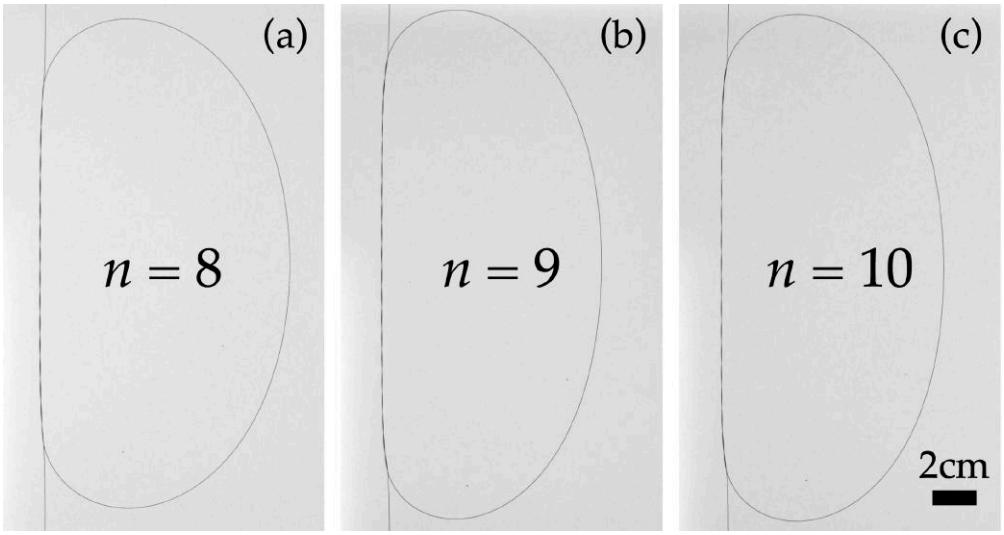

Figure S2: Representative photographs for knots on a Nitinol rod (properties defined in the main text), at high values of the unknotting number: (a) n = 8, (b) n = 9 and (d) n = 10. The pulling force is applied at the extremities of the top and bottom tails of the knot.

S5 Planarity of the loop

Throughout the manuscript, we have assumed the shape of the loop to be planar, which deserves experimental validation. In Fig. S3, we present representative photographs of the knots showing different views (in-plane, $y-z$, and out-of-plane, $x-z$) with two extreme cases for the unknotting number: (a) $n=1$ and (b) $n=10$. We define ψ as the angle created by the loop with respect to the $z-y$ plane (see Figs. S3a2,b2). We find that $\psi = 2.7°$ for $n=1$ and $\psi = 4.0°$ for $n=10$ ($e=47$ cm in both cases). These small values of ψ negligibly small values of ψ supports the planarity assumption made during the derivation of the theoretical model.

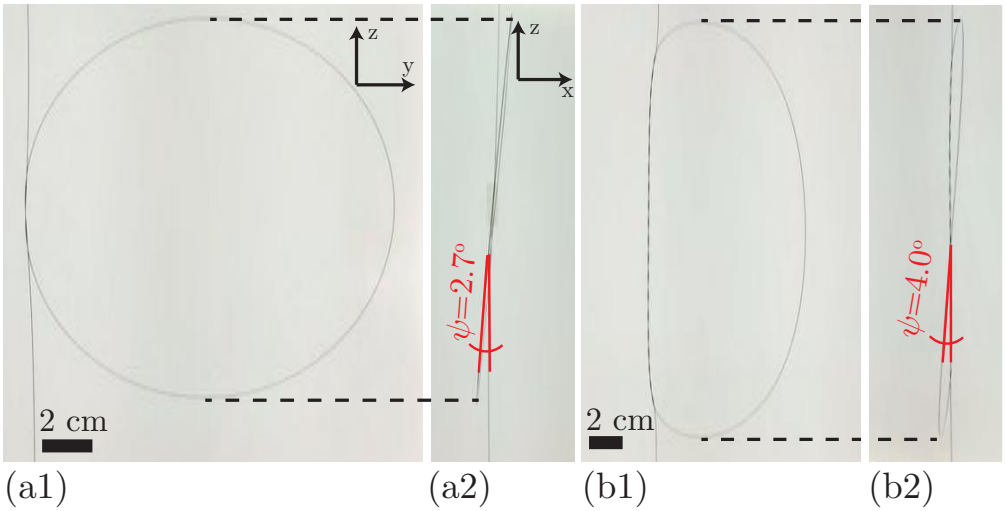

Figure S3: Orthogonal images of two knots: (a) $n=1, e=47$ cm, and (b) $n=10, e=47$ cm. In-plane ($y-z$) configurations are shown in (a1) and (b1), whereas out-of-plane ($x-z$) views are given in (a2) and (b2). The rod in the photograph is the same used in the experiments reported in the main manuscript.

S6 Validation of theory with different rods

Our theoretical model was compared against experiments using a single rod in Fig. 5 of the main text. For a rigorous test of the model, we now validate our theory using experiments with rods of 3 different radii,

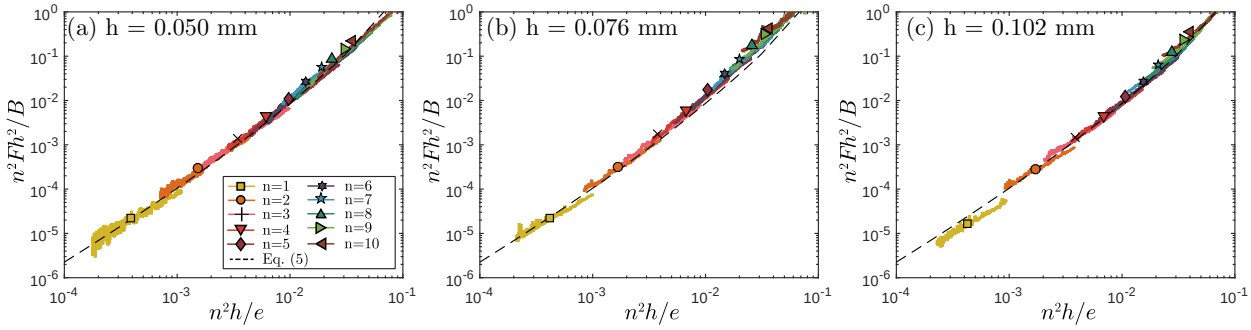

Figure S4: Force versus extension measurements, plotted using the dimensionless variables suggested by the theory, for rods with (a) $h=0.050$ mm, (b) $h=0.076$ mm, and (c) $h=0.102$ mm. Theoretical prediction (Eq. 5 of main text) is shown by the dashed line. Fig. 4 in the manuscript gives a plot with identical axes for $h=0.127$ mm.

h (and, therefore, different values of the bending rigidity, B). The rods had the same Young's modulus, $E = 67.50 \pm 0.25$ GPa, and we assumed the same value for the dynamic friction coefficient, $\mu = 0.119 \pm 0.001$, to be uniform across all rods. Recall that μ was measured through fitting in Fig. 2 of the manuscript. We performed force, F, vs. end-to-end shortening, e, measurements for each of the rods in the range $1 \leq n \leq 10$ of the unknotting number. The measurements have been plotted in Fig. S4 using the dimensionless variables suggested by the theory: $n^2 h/e$ vs. $n^2 F h^2/B$; reproduced below is Eq. (5) of the main text that gives the final form of the theoretical formulation:

$$n^2 \frac{h}{e} = \frac{1}{8\sqrt{3}\pi^2}\, g\left(\left[\frac{96\sqrt{3}\pi^2}{\mu} \cdot \frac{n^2 F h^2}{B}\right]^{1/3}\right). \tag{S4}$$

We find excellent quantitative agreement between experiments and theory, and thus confirms the universality of the theory within the limits mentioned in § S2.